Natural convective loops heat transfer scaling analysis

Franck Plouraboué, Martin Rudkiewicz, F. David, H. Neau, Gerald Debenest

Highlights

Natural convective loops heat transfer scaling analysis

Plouraboué, M. Rudkiewicz, F. David, H. Neau, G. Debenest

- Natural convective loops heat-exchanges are dominated by boundary-layer transfert
- The 3D buoyancy-driven flow-field is mainly unidirectional along the loop center-line
- The loop thermal efficiency fulfills a simple scaling with Graetz number, the exponent of which depends on the applied thermal conditions
- New scaling laws for Reynolds number versus Grashof relation are proposed which depends on the applied thermal conditions

Natural convective loops heat transfer scaling analysis

Plouraboué[1,*], M. Rudkiewicz[1], F. David[1], H. Neau[1], G. Debenest[1]

Abstract

Heat transfer arising in natural convective loops is analyzed. Combining 3D direct numerical simulations, unidirectional heat-transfer semi-analytical computations, scaling arguments and asymptotic analysis new universal scaling laws are proposed to account for dimensionless heat transfer behavior of natural convective loops. These scaling laws are successfully confronted with experimental measurements in various heating configurations. It is shown that the leading heat-transfer exchanges in natural convective loops are mainly dominated by boundary layers transfers, without noticeable influence of possibly complex 3D flow patterns found in the fluid flow. The proposed simple scaling laws constitute a progress over previously existing correlations which have disregarded the effect of boundary layers, heating configurations as well as fluid to solid variable diffusivity/conductivity.

Keywords: Convection in cavities, Buoyancy-driven instability, Coupled diffusion and flow, Natural convection, heat transfer, boundary layer

1. Introduction

Natural convective loops are passive thermal systems heated from bellow, cooled from above, where critical heating conditions produce a bifurcation above which a self-sustained "steady" flow is produced (Cf figure1a,b) breaking symmetry from rotating in one given direction. This stable limit-cycle, can nevertheless become unstable for higher heating forcing condition, and possibly reach a chaotic state from switching between various states [1, 2]. This first limit-cycle associated with the rotating periodic flow turns-out to be stable over a wide range of applied thermal conditions henc

*Corresponding author : fplourab@imft.fr

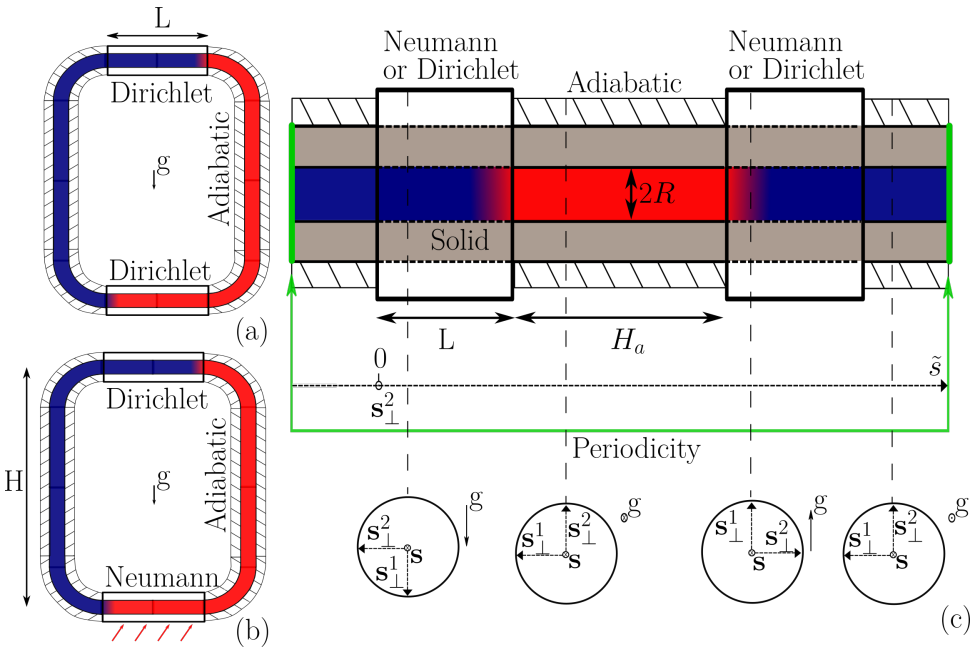

Figure 1: Natural convection loops having horizontal heated/cooled regions length $\tilde{L}$ ($\tilde{L} = L\tilde{R}$) and vertical height $\tilde{H}$ ($\tilde{H} = H\tilde{R}$), adiabatic length $\tilde{H}_a$ ($\tilde{H}_a = H_a\tilde{R}$) are considered in this study. 2D slices in the vertical mean-plane of the 3D loop are represented in (a-b). The interior fluid loop where thermal field iso-values drawed from hot (red) to cold (blue), has circular section of radius $\tilde{R}$ in the transverse plane (Cf bottom c). (a) Dirichlet/Dirichlet configuration (b) Neumann/Neumann one. (Top c) Deployed loop along the centerline periodic coordinate s. In 3D simulations provided in §2 the solid conduction is ignored (infinite solid conductivity limit) so that boundary conditions are directly applied at the fluid edge.

e producing a self-sustained buoyancy-driven steady flow interesting for heat transfer. This is a cooling flow without any pump, a so-called passive exchanger. These natural convective loops are thus ubiquitous heat exchangers in various applicative contexts such as nuclear plants [3, 4, 5], passive housing thermal exchangers, solar heaters [6], geothermal processes [3]. In these contexts several well-established correlations have been proposed to set-up and design the exchanges properties [7, 4]. These correlations produce a sensible power-law relation between the convective Reynolds number $Re = \tilde{W}_s 2\tilde{R}/\nu$ based upon the steady average velocity $\tilde{W}_s$, pipe/tube radius $\tilde{R}$, fluid kinematic viscosity ν and the Grashof number $Gr = 8\beta g \Delta\tilde{T}_h \tilde{R}^3/\nu^2$ related to fluid density ρ, gravity acceleration g, thermal expansion coefficient β and the reference forced temperature difference $\Delta\tilde{T}_h = \tilde{T}_H - \tilde{T}_C$ between the lower hot-pipe temperature $\tilde{T}_H$ and the cold bottom one $\tilde{T}_C$ in the case of Dirichlet type boundary conditions, or, in Neumann/Dirichlet case $\Delta\tilde{T}_h = \phi_w \tilde{R}/k_f$ where $\phi_w[W.m^-2]$ is the heat flux surface density, and $k_f\,[W.m^{-1}K^{-1}]$ the fluid thermal conductivity. Also more seldomly used in the literature three relevant non-dimensional parameters are interesting to consider : (i) the Péclet number $Pe = RePr$, closely related with the Reynolds number by the Prandtl number $Pr = \nu/\alpha_f$, with α_f the fluid thermal diffusivity related to its thermal conductivity k_f and specific heat c_p by $\alpha_f \equiv k_f/\rho_f c_p$ (ii) the Boussinesq number $Bo = GrPr^2$ (iii) and the Graetz number $G_{ra} = Pe\tilde{R}/\tilde{L}$, $\tilde{L}$ being the horizontal length of the loop. Although partially based upon energy balance and rational derivation, previous correlations derived in the literature have disregarded the effect of boundary layers for considering one-dimensional modeling only [8, 3, 9]. Also, all produced correlations have ignored both the significance of the applied boundary conditions in the loop.

Hence, in this contribution we revisit this problem. §2 analyses the generated flow field and transfer in a natural convective loop from 3D numerical simulations. §3 considers the modeling of unidirectional flow with generalized Graetz mode decomposition, the use of which permits to obtain a quasi-analytical solution for the 2D (axi-symmetric) temperature field. One outcome obtained in §3.3 is the evaluation of loop's exchanger efficiency, given by the dimensionless ratio between the averaged temperature difference $\Delta\tilde{T}$ between the outlet heated temperature at $\tilde{s} = \tilde{L}$ and the inlet cold one at $\tilde{s} = 0$, i.e $\Delta\tilde{T} = \langle\tilde{T}_f\rangle(\tilde{L}) - \langle\tilde{T}_f\rangle(0)$ ($\langle\rangle$ stands for cross-section average inside the circular loop), and the reference forced temperature difference $\Delta\tilde{T}_h$, i.e $\mathcal{E} = \Delta\tilde{T}/\Delta\tilde{T}_h$. The large Péclet asymptotic behaviour of $\mathcal{E}$ is further analyzed within a boundary layer analysis in §3.4. §4 then discusses the com-

parison between the resulting asymptotic predictions for relations between Re (or Pe), Gr (or Bo) and $\mathcal{E}$ confronted with experimental data both taking into account the heating configuration and the conductivity heterogeneity of fluid and solid.

2. Numerical study of 3D natural convection loop flow

The purpose of this section is to investigate the relevance of 3D flow field and geometry for heat-transfer in natural convective loops previously analyzed in the litterature. In most considered loops the aspect ratio between the inner tube radius and the loop's corner radius of curvature was small, so that 3D effects are expected to be moderate in this context. For this, finite-volume 3D simulations have been performed in a 3D domain similar to figure 1a for the configuration studied in [10] the details of which is given in table 1. The open-source software Saturne [11] has been used with dimensional formulation (using tilde fields) so as to permit a better comparison with experiments over a wide range of relevant Grashoff number, i.e from $Gr = 7.10^3$ to $Gr = 5.10^6$.

In these simulations boundary conditions are directly applied at the fluid flow frontier without considering conduction effects. Incompressible, non-stationnary, Boussinesq buoyancy-driven Navier-Stokes equations for velocity field $\tilde{\mathbf{u}}_f$, pressure $\tilde{p}$, temperature $\tilde{T}$, are solved in the 3D domain depicted in figure 1a associated with the Dirichlet/Neumann configuration

$$\rho\frac{\partial\tilde{\mathbf{u}}_f}{\partial t} + \rho\nabla\tilde{\mathbf{u}}_f\cdot\tilde{\mathbf{u}}_f = -\nabla\tilde{p} + \beta\rho\mathbf{g}(\tilde{T}-\tilde{T}^\star) + \mu\nabla^2\tilde{\mathbf{u}}_f, \tag{1}$$

whereby the fluid density and viscosity have been linearized around their value at reference temperature $\tilde{T}^\star$, i.e $\rho(\tilde{T}^\star)\equiv\rho$, $\mu(\tilde{T}^\star)\equiv\mu$, and β is the thermal expansion coefficient. $\tilde{T}^\star$ is provided by a shift from the imposed cold temperature $\tilde{T}_C$, i.e $\tilde{T}^\star = \tilde{T}_C + \Delta\tilde{T}^\star/2$ where $\Delta\tilde{T}^\star$ is the temperature drop gained from heat flux, i.e $\rho\tilde{W}_s\pi\tilde{R}^2c_p\Delta\tilde{T}^\star = \phi_w 2\pi R_0 L$ where the longitudinal velocity $\tilde{W}_s$ is related to the viscous pressure drop $\Delta\tilde{P}$ from $\tilde{W}_s = \Delta\tilde{P}\tilde{R}^2/(8\mu\tilde{L}_t)$ with the $\tilde{L}_t = 2(\tilde{L}+\tilde{H}_a)$ the total lenght of the heat loop along s. The pressure drop $\Delta\tilde{P}$ is compensated by buoyancy effects so that $\Delta\tilde{P} = \rho g\beta\Delta\tilde{T}^\star H$, leading to

$$\Delta\tilde{T}^\star = \sqrt{16\frac{\phi_w\mu\tilde{L}_t L R_0}{\rho^2\beta c_p g\tilde{H}\tilde{R}^4}}. \tag{2}$$

Navier-Stokes equations are coupled with the energy transport equations

$$\frac{\partial \tilde{T}}{\partial t} + \nabla \cdot (\tilde{\mathbf{u}}_f \tilde{T} - \alpha_f \nabla \tilde{T}) = 0, \tag{3}$$

where thermal diffusivity $\alpha_f = k_f/\rho c_p$ is related to thermal fluid conductivity k_f and fluid specific heat capacity c_p. No-slip boundary conditions are applied at the fluid domain edges. Also, at these edges, three distinct temperature boundary conditions are considered (i) imposed cold temperature T_C at Γ_D (ii) heated region at Γ_N (iii) adiabatic condition at Γ_A i.e

$$\tilde{T}\Big|_{\Gamma_D} = \tilde{T}_C \qquad \& \qquad k_f \nabla \tilde{T} \cdot \mathbf{n}\Big|_{\Gamma_N} = \phi_w \qquad \& \qquad \nabla \tilde{T} \cdot \mathbf{n}\Big|_{\Gamma_A} = 0 \tag{4}$$

The loop boundary is hence decomposed into two parts : thermally active regions where the loop is either heated or cooled and passive adiabatic ones where zero heat-flux is imposed. The domain itself is split in three regions : horizontal heated/cooled ones, bended parts, and vertical adiabatic ones. All thermo-physical quantities are taken for water at temperature $\tilde{T}^\star$. A 3D mesh-grid is generated from a 2D mesh extrusion. Local refinements of the grid have been performed in the bended regions and in the boundary layers so as to correctly capture temperature gradients. A mesh-refinement sensitivity analysis has been performed to reach less than 0.5% difference of the presented results. A time-stepping approach is adopted starting from a uniform initial condition. Then, imposing the prescribed boundary conditions, the solution converges toward a stable limit-cycle steady-state. A criteria to the convergence toward this self-rotating steady flow is found close within less than 0.04% of its previous value, i.e. the computation is stopped when finding temperature/pressure/velocity $\mathcal{L}^2$ residual variations from one times-step to the following lower than 4.10^{-4}. The numerical results are now analyzed in order to quantify the deviation from a one dimensional unidirectional flow of the 3D components one.

First, the hot to cold temperature difference $\Delta\tilde{T}$ obtained from numerical simulations are compared with the experimental results of [10] in table 1. The agreement obtained over these temperature differences is reasonnable (from 23 to 28 %) albeit not perfect. This difference might be attributable to idealized boundary conditions in the modeling side, whilst, at the same time, hardly controllable in experiments. This motivates a deeper analysis of the influence of solid conduction performed in the next section.

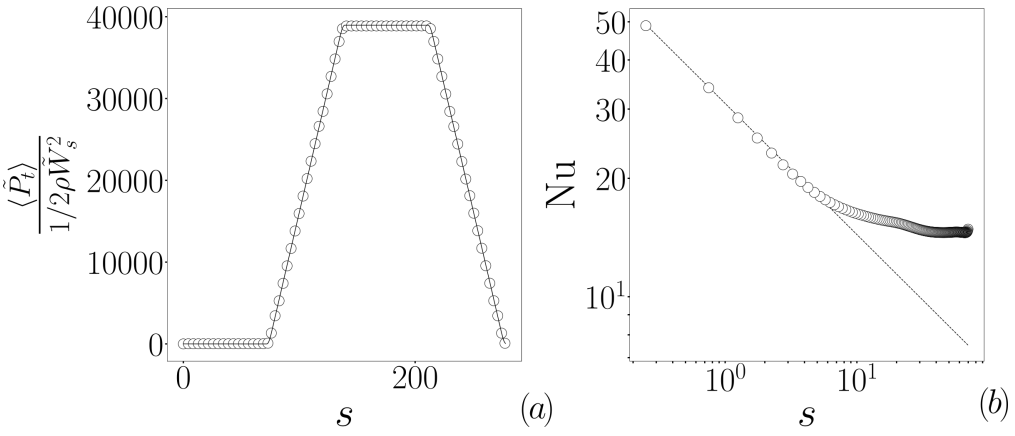

Figure 2: (a) Average pressure and variations along the center-line axis s inside each cross-sections of the heat loop. The static buoyancy pressure is superposed with continuous lines.(b) Cross-sectional averaged Nusselt number versus the dimensionless loop centerline distance s. A Lévêque behavior $Nu \sim s^{-1/3}$ is depicted with dotted lines.

$2\pi\tilde{R}_0\tilde{L}\phi_w[W]$	Re	$\Delta\tilde{T}[K]$ Exp	$\Delta\tilde{T}[K]$ CFD
300	317	16	11.4
400	354	19.5	14.9
500	378	22.5	17.1
700	441	27.2	20.3

Table 1: Comparison between the reported experimental temperature difference (experimental set-up MTT-1) of [10] and CDF ones. Reynolds number have been estimated from an energy balance on the heater [12], i.e. $Re = 4\pi\tilde{R}_0\tilde{L}\phi_w\tilde{R}/\rho_f c_p \Delta\tilde{T}\nu$. The loop parameters are $\tilde{R} = 0.01$m, $\tilde{L}_H = 0.72$m, $\tilde{L}_C = 0.6$m, $\tilde{H} = 0.637$m, $\tilde{H}_a = 0.759$m. The total heat flux is $2\pi\tilde{R}_0\tilde{L}\phi_w$.

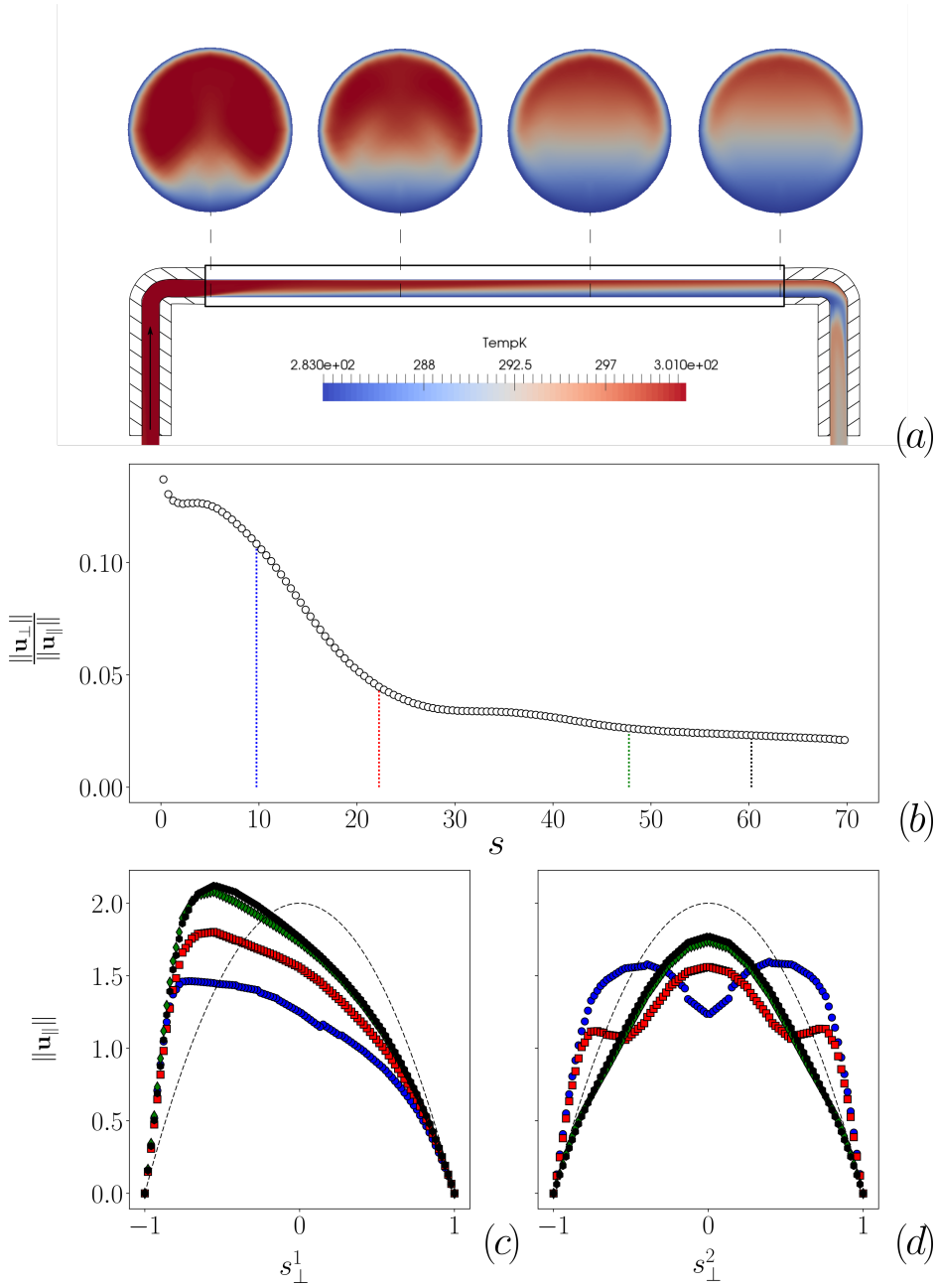

Figure 3: 3D Numerical simulations of natural convection stationary flow within a Dirichlet/Neumann thermal loop. (a-top) 2D temperature field in the transverse plane at various dimensionless axial distance s from the top-left of the loop. (a-bottom) 2D temperature field into the loop longitudinal plane. (b) Longitudinal to transverse flow velocity components ratio along the center-line coordinate s. (c) Radial velocity profile along directions direction $s^1_\perp$ (parallel to gravity) in the iso-s cross-section (Cf figure 1c) have been extracted. (d) same convention as (c) for direction $s^2_\perp$ (perpendicular to gravity).

The influence of 3D effects on the surface-averaged pressure drop variations along the loop are first considered. Figure 2 compares the pressure variations along the curvilinear axial coordinate s along the loop center-line with the static pressure associated with the buoyancy Boussinesq static term. This results shows a poor influence of other contributions to pressure variations i.e. viscous dissipation in bended regions (the so-called singular perturbation on pressure drop) or inertial pressure drop in the tube. Secondly, the temperature non-axi-symmetry and the resulting 3D velocity are illustrated and analyzed in figure 3. The temperature field (figure 3a) display a clear, axi-symmetric thin boundary layer structure along the circular tube periphery, whereas in the center, a top-to-bottom asymmetry is found. The non-axial component of the velocity field are also analyzed along the loop in figure 3, the relative amplitude of which are compared to the axial ones. A 10 % maximal variations of non-axial components relative to axial ones are found either within the straight portions of the loop, or in the heated/cooled regions. Furthermore, in average along centerline s the transverse velocity amplitude represents less than 5% of the longitudinal velocity. Also, deviations from Poiseuille flow of the longitudinal velocity component $\tilde{W}(r) = 2\tilde{W}_s(1 - (\tilde{r}/\tilde{R})^2)$ have been quantified in figure 3 at various distance from the entrance of the upper cooled region (i.e $10, 22.5, 47.5$ and 60 dimensionless diameter units). Since the 3D longitudinal velocity profiles are not axi-symmetric, two profiles (in the plane perpendicular to the center-line coordinate s (Cf figure 1c) have been extracted in the direction parallel to gravity ($s^1_\perp$) or perpendicular to it ($s^2_\perp$). A clear buoyancy driven, gravity-enhanced a-symmetric longitudinal velocity profile is visible in the left-bottom figure 3 along $s^1_\perp$. The profile a-symmetry is enhanced along the longitudinal direction increasing along the centre-line coordinate s. On the contrary, neither symmetric breakage of the velocity profile nor a-symmetry increase along s are found along $s^2_\perp$ profiles in figure 3's right-bottom. There, it is interesting to observe that the fluid boundary-layers effect at the entrance clearly decay along s leading to a closely parabolic profile far from it. Since both temperature and velocity display boundary layers, there are worth of a careful investigation. Figure 2 display the cross-sectional integrated transfer from evaluating the local Nusselt number along the curvilinear center-line coordinates s. As expected, heat transfer is decreasing from the entrance of the heated zone, down along the channel. A $s^{-1/3}$ decay of the local heat transfer is more precisely shown in figure 2, as expected from Lévêque approximation [13]. This behavior of the heat transfer indicates the dominant

effect of boundary layers on heat exchanges. This observation thus weakens the relevance of buyancy effects shown for velocity profiles to heat transfer. Since most of the transfer is controlled by thin regions near the solid boundary, the a-symetry of the velocity profile is not expected to impact much the near-wall radial temperature gradients.

Finally it is interesting to mention that since Saturne has embedded tabulated laws, numerical simulations using real water thermo-physics properties with temperature varying density, viscosity, specific heat capacity have also been produced and compared with the hereby discussed Boussinesq approximation results. A poor difference lower than 2% have been found between both. For this reason, the Boussinesq approximation has been kept as a relevant framework in the following sections. Furthermore, since a boundary-layer dominated heat transfer has been found from 3D simulations, the following section is further analyzing the expected predictions from heat-transfer resulting only from convection-diffusion arising within a axially invariant velocity profile ignoring the effect of transverse velocity components been small compared to longitudinal ones. Thus, we now proceed to the further analysis of the temperature field within unidirectional dimensionless flow field $\mathbf{u}_f = (0, 0, w_f(r))$ with $w_f(r) = \tilde{W}(r)/\tilde{W}_s$, now taking into account (possibly heterogeneous) conductive effects in the solid. Next section develops the leading order analysis of the bended-loop in the limit of asymptotically small pipe radius to loop radius of curvature ratio.

3. Unidirection convective exchanges in natural convection loop

3.1. Dimensionless formulation

As mentioned in the introduction the relevant dimensionless numbers in this context are Péclet number $Pe = \tilde{W}_s 2\tilde{R}/\alpha_f$ and Graetz number $G_{ra} = Pe\tilde{R}/L$. Rescaling the radial and axial coordinates $\tilde{r}$, $\tilde{z}$, $\tilde{s}$, $\tilde{L}$,$\tilde{H}_a$, & $\tilde{H}$ by $\tilde{R}$ (so that the fluid/solid interface Γ is at $r = 1$ whereas external boundary conditions Γ_A, Γ_D, Γ_N are set at $r = R_0 \equiv \tilde{R}_0/\tilde{R}$), the velocity by $\tilde{W}_s$, then, stationary dimensionless energy balance for the dimensionless fluid temperature T_f reads

$$\frac{1}{2} w_f(r) \frac{\partial T_f}{\partial s} - \frac{1}{Pe} \nabla^2 T_f = 0, \tag{5}$$

with dimensionless velocity $w_f(r) = 2(1 - r^2)$. Distinct conductive properties of solid walls within each compartment (i.e. cooled or heated region,

adiabatic regions) of the loop are considered. For each solid i, an harmonic temperature field associated with stationary conduction is prescribed for the dimensionless solid temperature T_s

$$\nabla^2 T_s = 0. \tag{6}$$

Continuity of temperature and fluxes are prescribed between fluid and solid domains

$$T_f\Big|_\Gamma = T_s\Big|_\Gamma \qquad \& \qquad \frac{\partial T_f}{\partial r}\Big|_\Gamma = \kappa \frac{\partial T_s}{\partial r}\Big|_\Gamma, \tag{7}$$

with $\kappa = k_s/k_f$ being the dimensionless solid to fluid conductivity ratio. In the following the field w is introduced being $w = w_f(r)/2$ in the fluid and $w = 0$ in the solid for $1 < r < R_0$. At external solid wall, either an adiabatic (homogeneous Neumann), Dirichlet or a constant heat flux (constant Neumann) are prescribed. Two distinct dimensionless temperature are thus considered. In the case of Dirichlet/Diriclet configurations (i.e D/D case) dimensionless $T = (\tilde{T} - \tilde{T}_C)/(\tilde{T}_H - \tilde{T}_C)$ is considered leading to dimensionless boundary conditions

$$\frac{\partial T_s}{\partial r}\Big|_{\Gamma_A} = 0 \qquad \& \qquad T_s\Big|_{\Gamma_D^C} = 0 \qquad \& \qquad T_s\Big|_{\Gamma_D^H} = 1, \tag{8}$$

where Γ_D^C and Γ_D^H are where the cold temperature $\tilde{T}_C$ and the hot one $\tilde{T}_H$ are prescribed. In the Dirichlet/Neumann case (i.e D/N case), $T = \phi_w(\tilde{T} - \tilde{T}_C)/(k_f \tilde{R})$ and dimensionless boundary conditions read

$$\frac{\partial T_s}{\partial r}\Big|_{\Gamma_a} = 0 \qquad \& \qquad T_s\Big|_{\Gamma_D} = 0 \qquad \& \qquad \kappa \frac{\partial T_f}{\partial r}\Big|_{\Gamma_N} = 1. \tag{9}$$

3.2. Semi-analytical solutions

Problem (5)-(8) & (5)-(9) can be solved by separation of variables using generalyzed Graetz modes decompositions [14, 15]. For homogeneous boundary conditions there is an orthogonal base decomposition upon discrete radial modes $\Theta_n(r)$ which fulfill the following radial problem in both fluid and solid domains

$$\kappa \left(\nabla_r^2 + \lambda_n^2\right) \Theta_n = \lambda_n w(r) Pe \Theta_n, \tag{10}$$

where ∇_r^2 stands for the radial part of the Laplacien operator. These modes are denoted with an upper D for Dirichlet when they fulfill boundary condition $\Theta_n^D(R_0) = 0$ or N for Neumann in the case $\partial_r \Theta_n^N(R_0) = 0$. General

solutions for non-homogeneous boundary conditions of Dirichlet, Neumann have been derived in [14, 16, 17]. In each stretch of the loop, having non-homogeneous constant boundary conditions, solutions (taking in each case the origin $s = 0$ of axial coordinate as the entrance of the boundary condition stretch) are provided. These solutions are decomposed into a general solution associated with uniform boundary conditions, and a particular one taking care off the non-homogeneous boundary condition (uniform in our case), the amplitude of which is given by $\alpha_n^{D,N}$ [15]

$$\alpha_n^D = -\frac{2\pi R_0 \kappa}{\lambda_n^2} \frac{d\Theta_n^D}{dr}\Big|_{R_0} \quad \& \quad \alpha_n^N = \frac{2\pi R_0}{\lambda_n} \Theta_n^N\big|_{R_0}. \tag{11}$$

3.2.1. Dirichlet/Dirichlet case

In this case, since the adiabatic regions do not play a role in the solid/fluid heat transfer, we disregard their role, and consider a succession of hot/cold temperature boundary conditions i.e

$$T(R_0, s)\Big|_{0<s<L} = 1 \qquad \& \qquad T(R_0, s)\Big|_{L<s<2L} = 0 \tag{12}$$

The solution reads

$$T(r,s) = \Pi(\frac{s+L/2}{L}) + \sum_{n>0} x_n^D \Theta_n^D e^{\lambda_n^D s} + \sum_{n<0} x_n^D \Theta_n^D e^{\lambda_n (s-2L)} + \sum_{n\in\mathbb{Z}^\star} \alpha_n^N \, c_n(s) \Theta_n^D \tag{13}$$

with $\Pi(s)$ is the rectangular function equal to one between $s = \pm 1/2$ and $c_{\pm n}(s)$ functions

$$c_n(s) = -\left(H(s) - H(s-L)e^{-\lambda_n L}\right) e^{\lambda_n s} \tag{14}$$

$$c_{-n}(s) = \left(H(s)e^{-2\lambda_{-n}L} - [1 - H(s-L)]e^{-\lambda_{-n}L}\right) e^{\lambda_{-n}s}, \tag{15}$$

with $x_{\pm n}^D$ amplitudes given by

$$x_n^D = \alpha_n^D \frac{1 - (1 - e^{-\lambda_n L})e^{2\lambda_n L}}{1 - e^{2\lambda_n L}}, \tag{16}$$

$$x_{-n}^D = \alpha_{-n}^D \frac{1 - (1 - e^{\lambda_{-n} L})e^{-2\lambda_{-n} L}}{e^{2\lambda_{-n} L} - 1}, \tag{17}$$

and for $n \in \mathbb{N}^\star$. From the numerical viewpoint, the behavior of (13) solution to mode truncation is not very favorable, so that, ones should alternatively

consider regularized boundary conditions (e.g erf-function shapes), for which some alternative analytical solutions using generalized Graetz modes could similarly be deduced from [15], the mode-convergence of which better behaves.

3.2.2. Dirichlet/Neumann case

In this case, boundary conditions at the solid surface are given by

$$T(R_0,s)\Big|_{0<s<L} = 0 \quad \& \quad \frac{\partial T(R_0,s)}{\partial r}|_{-(L+2H_a)<s<-(L+H_a)} = 0 \tag{18}$$

$$\kappa\frac{\partial T(R_0,s)}{\partial r}|_{-(L+H_a)<s<-H_a} = 1 \quad \& \quad \frac{\partial T(R_0,s)}{\partial r}|_{-H_a<s<0} = 0. \tag{19}$$

The solution within the Dirichlet region $0 < s < L$ reads

$$T^D(r,s) = T_w + \sum_{n>0} x^D_{+n}\Theta^D_{n+}e^{\lambda^D_n s} + \sum_{n<0} x^D_{-n}\Theta^D_{-n}e^{\lambda_n(s-L)}. \tag{20}$$

whilst the solution in the non-homogeneous Neumann region $-(L+2H_a) < s < 0$ is

$$T^N(r,s) = \sum_{n>0} x^N_{+n}\Theta^N_n e^{\lambda_n(s+2s_0)} + \sum_{n<0} x^N_n\Theta^N_n e^{\lambda_n s} + \sum_{n\in\mathbb{N}^\star}\alpha_n c_n(s) - (s'+\frac{L}{2})\Pi(\frac{2s'}{L})\frac{R_0}{Pe}, \tag{21}$$

where we have introduced the translated coordinate $s' = s+s_0$ with $s_0 = (L+2H_a)/2$. Albeit analytical, this solution is not explicit for needing unknown amplitudes $x^{D,N}_{\pm n}$. These amplitudes are found from imposing continuity of temperature and fluxes between the beginning of the first adiabatic region at $s = -2s_0$ with Dirichlet region outlet at $s = L$ and between the end of the second adiabatic region at $s = 0$ with Dirichlet one at $s = 0$. Hence, minimizing functional

$$\begin{aligned} J[x^D_n, x^N_n] \;=\; & \int_0^1 \left[\left(T^D - T^N\right)^2 + \left(\frac{\partial T^D}{\partial s} - \frac{\partial T^N}{\partial s}\right)^2\right]_{\big|_{s=0}} r dr + \\ & \int_0^1 \left[\left(T^D_{\big|_{s=L}} - T^N_{\big|_{s=-2s_0}}\right)^2 + \left(\frac{\partial T^D}{\partial s}|_{s=L} - \frac{\partial T^N}{\partial s}|_{s=-2s_0}\right)^2\right] r dr \end{aligned} \tag{22}$$

one can find the linear system to be solved in order to find the unknown vector $[x^D_n, x^N_n]$, the detail of which is provided in Appendix §Appendix A.

3.3. Numerical results for the loop efficiency

From the computed temperature fields provided in previous sections, one can evaluate the loop's efficiency whose expression simplifies to $\mathcal{E} = \langle T_f \rangle(L) - \langle T_f \rangle(0)$ for dimensionless temperature. This efficiency has been evaluated in figure 4 for both D/D and D/N cases for rectangular loops with $L = H = H_a$ varying between 2 to 100, for various Péclet numbers from unity to one thousand. In each case, the variation of the efficiency with Péclet follows the same qualitative trend, i.e. a sharp increase for moderate Péclet values followed by a gentle decrease as observed in most heat-exchangers (e. g. [18]). This secondary decay can be collapsed into a single curve from using the Graetz number rather than the Péclet as illustrated in figure 4b,d. Furthermore, the inset of figure 4b,d also show that the decay of the efficiency follows an asymptotic power-law decay with Graetz number, the slope of which is distinct in the D/D case and D/N one. Hence, when $G_{ra} \gg 1$ the efficiency follows the simple scaling

$$\mathcal{E}^{D/D} = \mathcal{E}_0 \left(\frac{Pe}{L} \right)^{-1/3} \quad \& \quad \mathcal{E}^{D/N} = \mathcal{E}_0 \left(\frac{Pe}{L} \right)^{-2/3}. \tag{23}$$

Note that since $R = 1$ for the dimensionless internal radius, the Péclet to Graetz relation simplifies to $G_{ra} = Pe/L$. The respective values of this power-law decay are further analyzed in the next section within an asymptotic analysis. The prefactor $\mathcal{E}_0$ of this power-law depends on the various conductivity ratios of the loop. For a loop having solid to fluid conductivity ratio $\kappa = k_s/k_f$, the asymptotic regime $G_{ra} \gg 1$ is further investigated. For this, in the D/D case the quantity $\mathcal{E}_0 \equiv \mathcal{E} G_{ra}^{1/3}$ has been analyzed in figure 5. One can observe on figure 5a that this prefactor very weakly changes within large variations of the Péclet number, as expected from (23). Furthermore, when considering the variation of this prefactor in a large range of variations of conductivity ratio κ parameter, a significant variation is found, with distinct asymptotic behaviors. For $\kappa \to \infty$, one can see in figure 5b that $\mathcal{E}_0$ reaches a plateau value, associated with the limit of a perfectly conductive solid (analysed in the next section). On the other hand, in the limit $\kappa \ll 1$, one finds a linear decay $\mathcal{E}_0 \sim \kappa$ (a fit capturing both trends is provided in figure 5's legend).

3.4. Boundary layer analysis

Now considering the local boundary layer dimensionless thickness $\delta = Pe^{-1/3} \ll 1$ following [13], the dimensionless longitudinal velocity $w(r)$

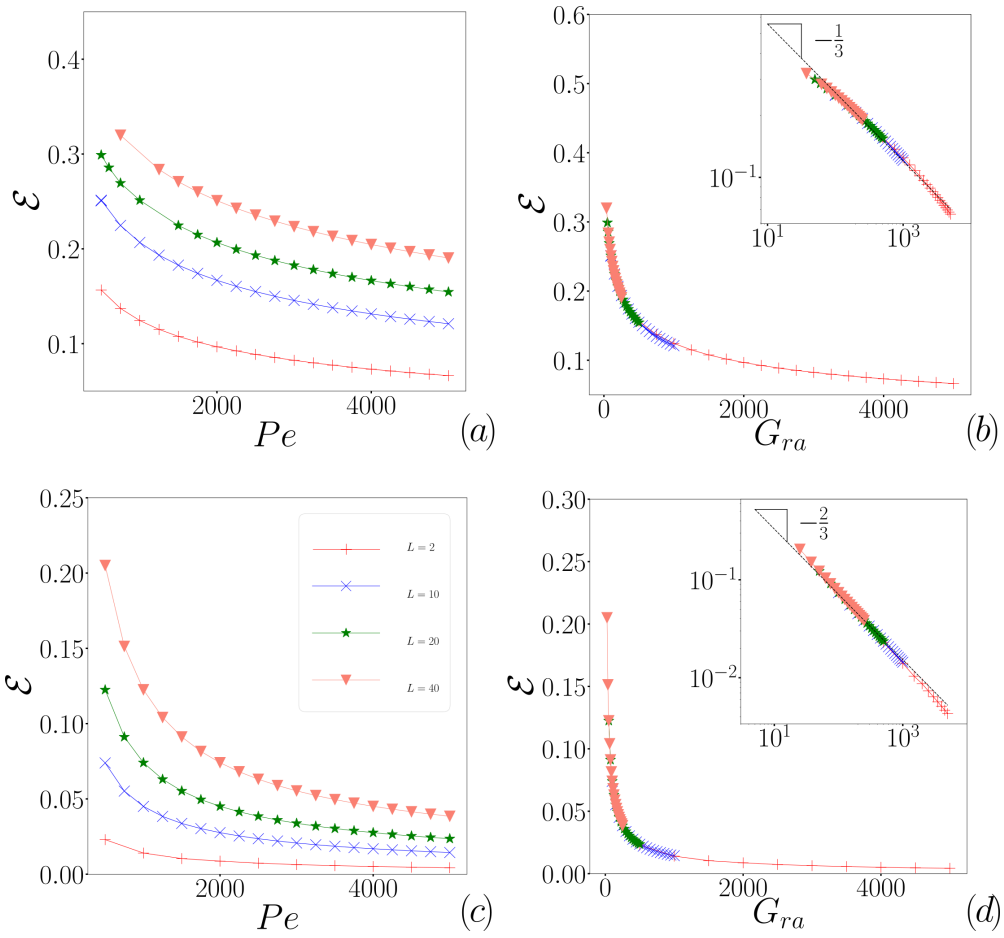

Figure 4: Efficiency of the loops computed from $\mathcal{E} = \Delta\tilde{T}/\Delta\tilde{T}_h = \Delta T$. (a-b) Diriclet/Diriclet case. (c-d) Dirichlet-Neumann case.

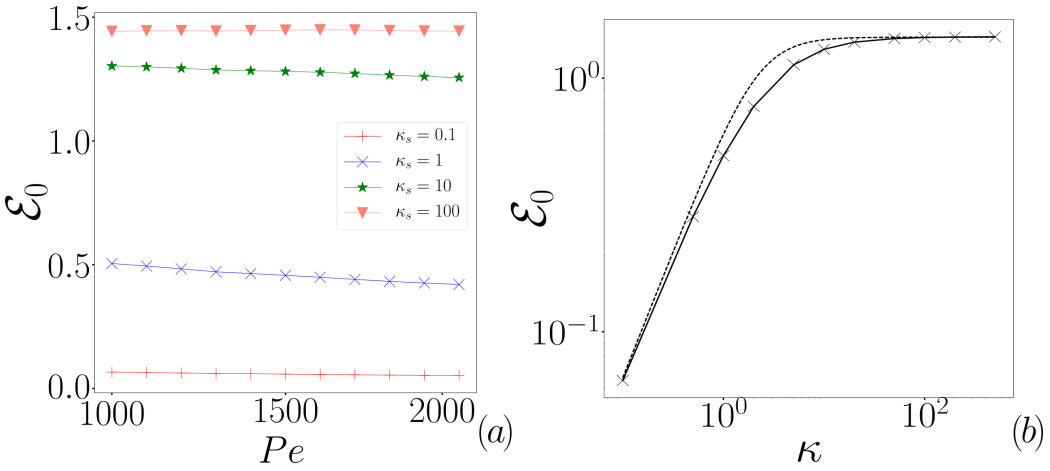

Figure 5: (a) $\mathcal{E}_0$ prefactor defined in (**??**) variation versus Pe number. (b) Continuous line is $\mathcal{E}_0$ versus conductivity ratio κ. Dotted lines provide a fit of this numerical result with the following fitting function $1.45\frac{\kappa/2.2}{\sqrt{1+(\kappa/2.2)^2}}$. A loop of dimensionless length $L = 4$ and $R_0 = 6/5$ has been chosen here.

nearby the wall, can be expressed with near wall outer variable $Y = 1 - r$, or inner one $y = Y/\delta$, so that $w_f(r)/2 = (1 - r^2) = Y(2 - Y) = \delta y(2 - \delta y)$ exhibiting an approximately linear behavior in the boundary layer where (5) then leads to $Pe\delta y\partial_s T \sim Pe\delta \sim (1/\delta^2)\partial_y^2 T \sim (1/\delta^2)$ justifying the boundary layer dimensionless thickness scaling with Pe. In this section, since we wish to address the effect of the fluid boundary layer in the limit of large Péclet number we consider the limiting case on infinite solid conductivity $\kappa \to \infty$ for which the thermal boundary conditions are imposed at the fluid/solid interface.

3.4.1. Dirichlet/Dirichlet case

On the one hand, the leading order boundary layer dimensionless temperature T_{in}^0 deduced from (5) fulfills

$$2y\frac{\partial T_{in}^0}{\partial s} - \frac{\partial^2 T_{in}^0}{\partial y^2} = 0, \tag{24}$$

with, boundary condition $T_{in}^0(y = 0) = 1$, complemented with matching conditions with the dimensionless outer temperature T_{out}^0 such as $T_{in}^0(y \to \infty) = T_{out}^0(Y \to 0) \equiv T_{out}^0(0)$. It admits Lévêque self-similar solution introducing

self-similar variable $\mathcal{Y} = y/(9s/2)^{1/3}$ so that classical results is recovered [13],

$$T^0_{in}(\eta) = T^0_{out}(0) + (1 - T^0_{out}(0))\frac{3}{\Gamma(1/3)}\int_{\mathcal{Y}}^{\infty} \exp^{-t^3} dt \tag{25}$$

On the other hand, from (5), one can find that the leading-order outer field verifies $\partial_s T^0_{out} = 0$, i.e is invariant along s –this property holds, up to $O(\delta^3)$ corrections–. Since the efficiency $\mathcal{E} = \Delta\tilde{T}/(\tilde{T}_H - \tilde{T}_C) = \langle T_f\rangle(L) - \langle T_f\rangle(0)$ can be evaluated using boundary-layer leading-orders from

$$\begin{aligned}
\langle T_f\rangle(L) &= \int_0^{\delta L^{1/3}} T_{in}(y)(1-\delta y)dy + \int_{\delta L^{1/3}}^{1} T_{out}(Y)(1-Y)dY & (26)\\
&= \delta L^{1/3} + \int_{\delta L^{1/3}}^{1} T^0_{out}(Y)(1-Y)dY + O(\delta^2) & (27)
\end{aligned}$$

At $s = 0$, since $\partial_s T^0_{out} = 0$, one gets

$$\begin{aligned}
\langle T_f\rangle(0) &= \int_0^{\delta L^{1/3}} T_{out}(Y)(1-Y)dY + \int_{\delta L^{1/3}}^{1} T_{out}(Y)(1-Y)dY & (28)\\
&= T^0_{out}(0)\delta L^{1/3} + \int_{\delta L^{1/3}}^{1} T^0_{out}(Y)(1-Y)dY + O(\delta^2) & (29)
\end{aligned}$$

From (27) and (29), one finds that, in the D/D case, the loop efficiency scales as

$$\mathcal{E}^{D/D} = \langle T_f\rangle(L) - \langle T_f\rangle(0) = [1 - T^0_{out}(0)]\delta L^{1/3} + O(\delta^2) \sim (L/Pe)^{1/3} \tag{30}$$

This results is consistent with figure 4b inset behavior, i.e (23) scaling.

3.4.2. Dirichlet/Neumann case

In this case, the leading-order solution of the $O(1)$ boundary-layer problem (24) associated with homogeneous boundary condition $\partial_y T^0_{in}(y = 0) = 0$ is constant, i.e $T^0_{in} = T^0_{out}(0)$, given by the matching condition with the s-invariant, $\partial_s T^0_{out} = 0$, outer solution. Next order $O(\delta)$ correction also fulfills (24) with the non-homogeneous uniform boundary condition $\partial_y T^1_{in}(y = 0) = 1$ preventing a self-similar solution in this case, but for a linear profile $T^1_{in}(y) = y$ (Cf Appendix Appendix B for more details). Using (26) one finds in this D/N case

$$\langle T_f\rangle(L) = T^0_{out}(0)\delta L^{1/3} + \int_{\delta L^{1/3}}^{1} T^0_{out}(Y)(1-Y)dY + O(\delta^3), \tag{31}$$

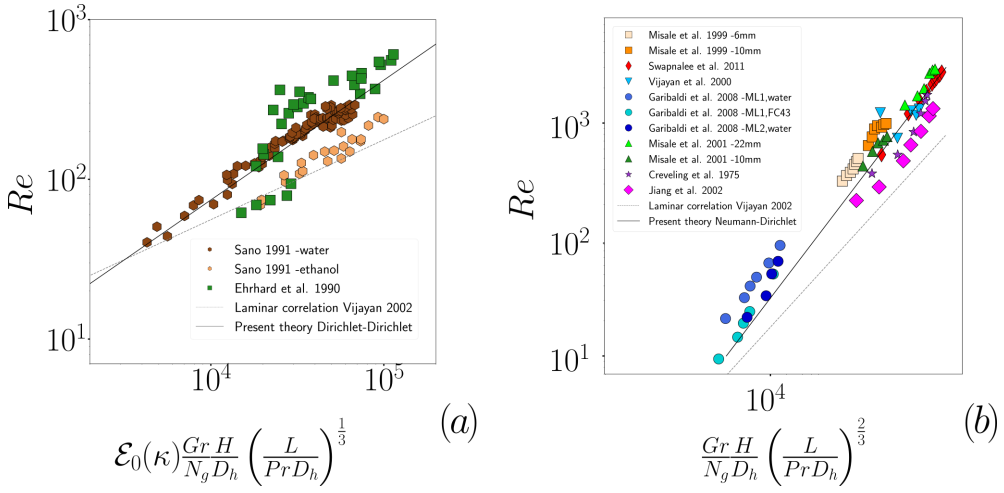

Figure 6: Reynolds number versus Grashof number for various experimental natural convection loops. Dotted lines are the correlation proposed in [4]. (a) D/D case. Continuous line is the D/D scaling (36) $Re \sim Gr^{3/4}$. (b) D/N case. Continuous line is the D/N scaling (36) $Re \sim Gr^{3/5}$.

and using definition (28),

$$\langle T_f \rangle(0) = T^0_{out}(0)\delta L^{1/3}(1-\frac{\delta}{2}L^{1/3})+\frac{\partial T^0_{out}}{\partial Y}(0)\frac{\delta^2}{2}L^{2/3}+\int_{\delta L^{1/3}}^{1} T^0_{out}(Y)(1-Y)dY+O(\delta^3), \tag{32}$$

From matching condition $\partial_Y T^0_{out}(0) = 1$ (Cf Appendix Appendix B for more details), one gets

$$\mathcal{E}^{D/N} = \langle T_f \rangle(L) - \langle T_f \rangle(0) = \frac{[T^0_{out}(0)-1]}{2}\delta^2 L^{2/3} + O(\delta^3) \sim (L/Pe)^{2/3} \tag{33}$$

Again, this is consistent with figure 4d inset behavior and (23) scaling.

4. Results

Balancing the fluid pressure including both viscous pressure drop and singular perturbation contributions associated with loop's corners (provided by ξ_s parameter) , with Archimedian one leads to

$$\beta\rho g\Delta\tilde{T}\tilde{H} = \frac{1}{2}\rho\tilde{W}_s^2(\frac{64}{Re}L_t + \xi_s), \tag{34}$$

Using previous dimensionless number definitions and dimensionless notation $N_g = (L_t + Re\xi_s/64)$ in (34) leads to the simple relation between the Grashof number Gr, the efficiency $\mathcal{E}$ and the Reynolds number Re

$$HGr\mathcal{E} = 32ReN_g. \tag{35}$$

Now using scalings (23) in (35) provides new scaling laws for the Re-Gr relation

$$D/D : Re \sim \left(\frac{Gr}{N_g} H (\frac{L}{Pr})^{1/3}\right)^{3/4} \quad \& \quad D/N : Re \sim \left(\frac{Gr}{N_g} H (\frac{L}{Pr})^{2/3}\right)^{3/5}. \tag{36}$$

Both scaling are tested upon experimental results of [10, 19, 20, 21, 12, 22] in figure 6. Figure 6 also depicts the correlations $Re \sim \sqrt{Gr}$ proposed by [4]. In the D/N case, the predicted slope of our scaling (36) (continuous line) compared to previous correlations ($Re \sim \sqrt{Gr}$) (dotted line) provides a better trend to the experimental points which have been gathered from numerous experimental configurations (having distinct loops dimensions, thermal conditions, as well as materials). The comparison between figure 6a and 6b trend, clearly shows that the experimental Re-Gr relation also depends on the applied sets of boundary conditions. To be specific, the experimental points collapsed into figure 6a show a $Re \sim Gr^{3/4}$ scaling (continuous curve) distinct from the $Re \sim Gr^{3/5}$ of figure 6b as well as from [4] correlation's $Re \sim Gr^{1/2}$. Thermal conditions, i.e boundary-conditions dependant behaviour of natural convective loops is an issue previously disregarded. Furthermore, it is worth observing that the data collapse obtained in figure 6 is not perfect, as also found in previous scaling analysis of the Reynolds-Grashof relation in natural convective loops [4, 23]. However, here, the data collapse has been improved from considering the all sets of parameters and dimensionless number given in (36), among whose prefactor $\mathcal{E}_0(\kappa)$ improved it significantly. This suggest that some other distinct features of specific experimental loops could be responsible for this imperfect data collapse, as for exemple, another additional solid (with a different conductivity) used in the adiabatic regions.

5. Conclusion

Natural convective loops are practical, sparce, pump-free boyency driven heat exchangers, heated from below and cooled from above. Above a critical Grashof number, and within a wide range of Gr, they display a stable,

self-sustained rotating flow. This work has investigated the origin of experimentally reported scaling-laws for the Reynolds-Grashof relation within these loops. Numerical simulations have permitted to analyze the 3D complex flow field resulting from both complex geometry and inertia. Albeit the flow-field significantly differs from a laminar unidirectional buyency driven Poiseuille flow, deviations from it are found poorly relevant to heat transfer, being dominated by entrance exchanges within boundary layers. This has motivated forthcoming efforts to analyse heat transfer in these loops within unidirectional flow approximation. Using a semi-analytical approach, the complete advection-diffusion-conduction transport problem (both in fluid and solid) has been solved using generalyzed Graetz-mode solutions. Studying the loop thermal efficiency, distinct and well-defined power-law scalings are found for the efficiency versus Graetz number relation in the large G_{ra} limit. These semi-analytical results have been complemented with an asymptotic analysis of heat transfer within boundary layers providing consistent scaling for the thermal efficiency. Using this efficiency scaling within a one-dimensional pressure balance within the loop leads to new scaling relationship for the Reynolds-Grashof relation dependant on the chosen set of applied thermal boundary conditions. These predictions have been convinsingly compared with experimental obervation collapsed into proper combination of dimensionless parameters. This analysis could help designing convective loop exchange's capabilities.

Acknowledgments

This work is under a CC-BY 4.0 licence. This work was supported by EDF and ANRT.

Appendix A. Dirichlet-Neumann linear problem

Let us first define matrix $\mathbf{P}^{\pm\pm}_{DD}$, from its elements $[\mathbf{P}^{\pm\pm}_{DD}]_{ij}$for $(i,j) \in \mathbb{N}^*$,

$$[\mathbf{P}^{\pm\pm}_{DD}]_{ij} = \int_0^1 \left(1 + \lambda^D_{\pm i}\lambda^D_{\pm j}\right) \Theta^D_{\pm i}\Theta^D_{\pm j} r dr. \tag{A.1}$$

Similarly $\mathbf{P}^{\pm\pm}_{DN}$ defined by

$$[\mathbf{P}^{\pm\pm}_{DN}]_{ij} = \int_0^1 \left(1 + \lambda^D_{\pm i}\lambda^N_{\pm j}\right) \Theta^D_{\pm i}\Theta^N_{\pm j} r dr, \tag{A.2}$$

Furthermore, for $(i,j) \in \mathbb{N}^*$, let us define diagonal matrices $\mathbf{D}_D^{\pm}(s)$ parametrized by s as

$$[\mathbf{D}_D^+]_{ij} = \delta_{ij} \exp^{\lambda_{+j}^D s} \quad , \quad [\mathbf{D}_D^-]_{ij} = \delta_{ij} \exp^{\lambda_{-j}^D (s-L)} \tag{A.3}$$

and $\mathbf{D}_N^{\pm}(s)$ as

$$[\mathbf{D}_N^+]_{ij} = \delta_{ij} \exp^{\lambda_{+j}^N s} \quad \& \quad [\mathbf{D}_N^-]_{ij} = \delta_{ij} \exp^{\lambda_{-j}^N (s+2s_0)} \tag{A.4}$$

with $2s_0 = L + 2H$. Now defining symmetric matrix $\mathbf{M}_1$ (associated with the top part of functionnal (22)) as

$$\mathbf{M}_1 = \begin{pmatrix} \mathbf{P}_{DD}^{++} & \mathbf{P}_{DD}^{+-}\mathbf{D}_D^-(0) & \mathbf{P}_{DN}^{++}\mathbf{D}_N^+(0) & \mathbf{P}_{DN}^{+-} \\ \cdots & \mathbf{D}_N^-(0)\mathbf{P}_{DD}^{--}\mathbf{D}_N^-(0) & \mathbf{D}_D^-(0)\mathbf{P}_{DN}^{-+}\mathbf{D}_N^+(0) & \mathbf{D}_D^-(0)\mathbf{P}_{DN}^{--} \\ \cdots & \cdots & \mathbf{D}_N^-(0)\mathbf{P}_{NN}^{++}\mathbf{D}_N^+(0) & \mathbf{D}_N^+(0)\mathbf{P}_{NN}^{+-} \\ \cdots & \cdots & \cdots & \mathbf{P}_{NN}^{--} \end{pmatrix} \tag{A.5}$$

and symmetric matrix $\mathbf{M}_2$ (associated with the bottom part of functionnal (22)) as

$$\mathbf{M}_2 = \begin{pmatrix} \mathbf{D}_D^+(L)\mathbf{P}_{DD}^{++}\mathbf{D}_D^+(L) & \mathbf{D}_D^+(L)\mathbf{P}_{DD}^{+-} & \mathbf{D}_D^+(L)\mathbf{P}_{DN}^{++} & \mathbf{D}_D^+(L)\mathbf{P}_{DN}^{+-}\mathbf{D}_N^-(-2s_0) \\ \cdots & \mathbf{P}_{DD}^{--} & \mathbf{P}_{DN}^{-+} & \mathbf{P}_{DN}^{--}\mathbf{D}_N^-(-2s_0) \\ \cdots & \cdots & \mathbf{P}_{NN}^{++} & \mathbf{P}_{NN}^{+-}\mathbf{D}_N^-(-2s_0) \\ \cdots & \cdots & \cdots & \mathbf{D}_N^-(-2s_0)\mathbf{P}_{NN}^{--}\mathbf{D}_N^-(-2s_0) \end{pmatrix}, \tag{A.6}$$

with, again, $-2s_0 = -L - 2H$. Unknown vector $\mathbf{X}$ is build from unknown amplitudes vectors $\mathbf{x}_{\pm}^D$ —resp -$\mathbf{x}_{\pm}^N$–whose components are $x_{\pm n}^D$ —resp -$x_{\pm n}^N$– from $\mathbf{X} = (\mathbf{x}_+^D, \mathbf{x}_-^D, \mathbf{x}_+^N, \mathbf{x}_-^N)^T$. Vectors $\mathbf{S}_{\pm}^N(s)$ are define from their components

$$\mathbf{S}_{\pm n}^N(s) = \alpha_{\pm n}^N c_{\pm n}(s) \tag{A.7}$$

with $c_{\pm n}(s)$ given in (16) and α_n^N in (11). Defining $\mathbf{R}_{\pm}^D$ vectors $\mathbf{R}_{\pm}^N$ with their components

$$\mathbf{R}_{\pm n}^D = \int_0^1 \Theta_{\pm n}^D r dr \qquad \& \qquad \mathbf{R}_{\pm n}^N = \int_0^1 \Theta_{\pm n}^N r dr, \tag{A.8}$$

with generalyzed Graetz modes Θ_n defined in (10). Vectors $\mathbf{B}_1$ is then defined as

$$\mathbf{B}_1 = \frac{2R_0 L}{Pe} \begin{pmatrix} \mathbf{D}_D^+(0)\mathbf{R}_+^D \\ \mathbf{D}_D^-(0)\mathbf{R}_-^D \\ \mathbf{D}_N^+(0)\mathbf{R}_+^N \\ \mathbf{D}_N^-(0)\mathbf{R}_-^N \end{pmatrix} + \begin{pmatrix} \mathbf{D}_D^+(0)\mathbf{P}_{DN}^{++}\mathbf{S}_+^N(0) + \mathbf{D}_D^+(0)\mathbf{P}_{DN}^{+-}\mathbf{S}_-^N(0) \\ \mathbf{D}_D^-(0)\mathbf{P}_{DN}^{-+}\mathbf{S}_+^N(0) + \mathbf{D}_D^-(0)\mathbf{P}_{DN}^{--}\mathbf{S}_-^N(0) \\ \mathbf{D}_N^+(0)\mathbf{P}_{NN}^{++}\mathbf{S}_+^N(0) + \mathbf{D}_N^+(0)\mathbf{P}_{NN}^{+-}\mathbf{S}_-^N(0) \\ \mathbf{D}_N^-(0)\mathbf{P}_{NN}^{-+}\mathbf{S}_+^N(0) + \mathbf{D}_N^-(0)\mathbf{P}_{NN}^{--}\mathbf{S}_-^N(0) \end{pmatrix}, \tag{A.9}$$

and

$$\mathbf{B}_2 = \begin{pmatrix} \mathbf{D}_D^+(L)\mathbf{P}_{DN}^{++}\mathbf{S}_+^N(-2s_0) + \mathbf{D}_D^+(L)\mathbf{P}_{DN}^{+-}\mathbf{S}_-^N(-2s_0) \\ \mathbf{D}_D^-(L)\mathbf{P}_{DN}^{+-}\mathbf{S}_+^N(-2s_0) + \mathbf{D}_D^-(L)\mathbf{P}_{DN}^{--}\mathbf{S}_-^N(-2s_0) \\ \mathbf{D}_N^+(-2s_0)\mathbf{P}_{NN}^{++}\mathbf{S}_+^N(-2s_0) + \mathbf{D}_N^+(-2s_0)\mathbf{P}_{NN}^{+-}\mathbf{S}_-^N(-2s_0) \\ \mathbf{D}_N^-(-2s_0)\mathbf{P}_{NN}^{+-}\mathbf{S}_+^N(-2s_0) + \mathbf{D}_N^-(-2s_0)\mathbf{P}_{NN}^{--}\mathbf{S}_-^N(-2s_0) \end{pmatrix}, \quad \text{(A.10)}$$

Assembling

$$\mathbf{M} = \mathbf{M}_1 + \mathbf{M}_2 \qquad \& \qquad \mathbf{B} = \mathbf{B}_1 + \mathbf{B}_2 \quad \text{(A.11)}$$

The linear system to be solved is finally :

$$\mathbf{M}\,\mathbf{X} = \mathbf{B} \quad \text{(A.12)}$$

Appendix B. Dirichlet-Neumann boundary layer analysis

Appendix B.1. Inner analysis

It is first interesting to provide the expansion of the radial Laplacian of the r.h.s of (5) in ther inner variable y

$$\frac{1}{(1-\delta y)}\frac{\partial}{\partial y}\left((1-\delta y)\frac{\partial}{\partial y}\right) = \frac{\partial^2}{\partial y^2} - \delta\frac{\partial}{\partial y} - \delta^2 y\frac{\partial}{\partial y} + O(\delta^3) \quad \text{(B.1)}$$

In the inner region, the temperature field is expended as

$$T_{in} = T_{in}^0 + \delta T_{in}^1 + \delta^2 T_{in}^2 + O(\delta^3) \quad \text{(B.2)}$$

At $O(1)$, (5) leads to

$$2y\frac{\partial T_{in}^0}{\partial s} - \frac{\partial^2 T_{in}^0}{\partial^2 y} = 0, \quad \text{(B.3)}$$

with boundary condition $\partial_y T_{in}^0(0) = 0$. The leading order solution then reads

$$T^0 = a_0^0 + a_1^0(\frac{y^3}{3} + s) \quad \text{(B.4)}$$

At $O(\delta)$, (5) with $w_f(r)/2 = \delta y(2-\delta y)$ provides

$$2y\frac{\partial T_{in}^1}{\partial s} - \frac{\partial^2 T_{in}^1}{\partial y^2} = y^2\frac{\partial T_{in}^0}{\partial s} - \frac{\partial T_{in}^0}{\partial y}, \quad \text{(B.5)}$$

associated with boundary condition $\partial_y T_{in}^1(0) = 1$. The first order solution is decomposed into a particular solution dealing with the non-zero boundary

condition and the r.h.s. of (B.5) and a general solution which is a copy of the leading order (B.4). Since the contribution associated with r.h.s. of (B.5) evaluated with (B.4) cancels out, one finds

$$T_{in}^1 = y + a_0^1 + a_1^1(\frac{y^3}{3} + s) \tag{B.6}$$

At $O(\delta^2)$, using (B.1)

$$2y\frac{\partial T_{in}^2}{\partial s} - \frac{\partial^2 T_{in}^2}{\partial y^2} = y^2\frac{\partial T_{in}^1}{\partial s} - \frac{\partial T_{in}^1}{\partial y} - y\frac{\partial}{\partial y}T_{in}^0, \tag{B.7}$$

with boundary condition $\partial_y T_{in}^2(0) = 0$. Again, the solution is decomposed into the general and particular ones, so that

$$T_{in}^2 = -\frac{1}{2}y^2 + a_1^0 y^3 + a_0^2 + a_1^2(\frac{y^3}{3} + s) \tag{B.8}$$

Appendix B.2. Outer analysis

The outer region temperature field is expended as

$$T_{out} = T_{out}^0(0) + O(\delta^3) \tag{B.9}$$

because up to $O(\delta^3)$ corrections, (5) with $w_f(r) = 2Y(2-Y)$ provides

$$\frac{1}{2}w_f(Y)\frac{\partial T_{out}^0}{\partial s} = 0. \tag{B.10}$$

Hence, the leading order outer temperature is independant of the axial coordinate s, so that $T^0(Y)$ which is both determined by the inlet profile and the matching. Since the inlet profile is $O(1)$, there is no $O(\delta)$ and $O(\delta^2)$ corrections to the outer solution.

Appendix B.3. Matching

Using the intermediate variable $\eta = y\delta^{1-\gamma} = Y\delta^{-\gamma}$ with $0 < \gamma < 1$, and expanding T_{out} in η leads to

$$T_{out} = T_{out}^0(0) + \eta\delta^\gamma\frac{\partial T_{out}^0}{\partial Y}(0) + \frac{1}{2}\eta^2\delta^{2\gamma}\frac{\partial^2 T_{out}^0}{\partial Y^2}(0) + ... \tag{B.11}$$

Expanding the inner solution leads to

$$\begin{aligned} T_{in} &= \frac{a_1^0}{3}\eta^2\delta^{3(\gamma-3)} + \frac{a_1^1}{3}\eta^2\delta^{3(\gamma-2)} + (\frac{a_1^2}{3} + a_1^0)\eta^3\delta^{(3\gamma-1)} \\ &\quad + a_0^0 + a_1^0 s + \delta(a_0^1 + a_1^1 s) + \eta\delta^\gamma - \frac{1}{2}\eta^2\delta^{2\gamma}\delta^2(a_0^2 + a_2^1 s) + ... \end{aligned}$$

Matching at $O(\delta^{3(\gamma-3)})$, $O(\delta^{3(\gamma-2)})$, $O(\delta^{3(\gamma-1)})$ gives $a_1^0 = a_1^1 = a_1^2 = 0$. Matching $O(1)$ and $O(\delta^\gamma)$ gives

$$a_0^0 = T_{out}^0(0), \qquad \& \qquad 1 = \frac{\partial T_{out}^0}{\partial Y}(0), \tag{B.12}$$

whilst matching $O(\delta)$ and $O(\delta^2)$ gives $a_0^1 = a_0^2 = 0$. This finally leads to

$$T_{in}^0 = T_{out}^0(0) + \delta y + O(\delta^3) \tag{B.13}$$

References

[1] P. Welander, On the oscillatory instability of a differentially heated fluid loop, J. Fluid Mech. 29 (1) (1967) 17–30.

[2] P. Ehrhard, U. Muller, Dynamical behaviour of natural convection in a single-phase loop, J. Fluid Mech. 217 (1990) 487–518.

[3] P. Vijayan, A. W. Mehta, K.S.and Date, On the steady-state performance of natural circulation loops, Int. J. Heat Mass Tran. 34 (9) (1991) 2219–2230.

[4] P. Vijayan, H. Austregesilo, Scaling laws for single-phase natural circulation loops, Nucl. Eng. Des. 152 (1) (1994) 331–347.

[5] N. Bordoloi, A. Sharma, H. Nautiyal, V. Goel, An intense review on the latest advancements of earth air heat exchangers, Renewable and Sustainable Energy Reviews 89 (2018) 261–280.

[6] V. T. Morgan, The overall convective heat transfer from smooth circular cylinders, in: T. F. Irvine, J. P. Hartnett (Eds.), Adv. Heat Transf., Vol. 11, Elsevier, 1975, pp. 199–264.

[7] M. Ishii, I. Kataoka, Scaling laws for thermal-hydraulic system under single phase and two-phase natural circulation, Nucl. Eng. Des. 81 (3) (1984) 411–425.

[8] D. N. Basu, S. Bhattacharyya, P. Das, Development of a unified model for the steady-state operation of single-phase natural circulation loops, Int. J. Heat Mass Tran. 62 (2013) 452–462.

[9] R. Saha, S. Sen, S. Mookherjee, K. Ghosh, A. Mukhopadhyay, D. Sanyal, Experimental and numerical investigation of a single-phase square natural circulation loop, J. Heat Transfer 137 (12) (08 2015).

[10] M. Misale, M. Frogheri, Influence of pressure drops on the behavior of a single-phase natural circulation loop: Preliminary results, Int. Commun. Heat Mass Transf. 26 (5) (1999) 597–606.

[11] Z. Shang, Performance analysis of large scale parallel CFD computing based on code Saturne., Comput. Phys. Commun. 184 (2013) 381–386.

[12] H. F. Creveling, J. F. De Paz, J. Y. Baladi, R. J. Schoenhals, Stability characteristics of a single-phase free convection loop, J. Fluid Mech. 67 (1) (1975) 65–84.

[13] W. M. Deen, Analysis of transport phenomena, Oxford University Press, 1998.

[14] C. Pierre, F. Plouraboué, Numerical analysis of a new mixed formulation for eigenvalue convection-diffusion problems, SIAM J. Appl. Math 70 (3) (2009) 658–676.

[15] C. Pierre, F. Plouraboué, Analytical properties of Graetz modes in parallel and concentric configurations, Meccanica 55 (8) (2020) 1545–1559.

[16] J. Bouyssier, C. Pierre, F. Plouraboué, Mathematical analysis of parallel convective exchangers with general lateral boundary conditions using generalized graetz modes, Math Models Methods Appl Sci 24 (4) (2014) 627–665.

[17] C. Pierre, J. Bouyssier, F. de Gournay, F. Plouraboué, Numerical computation of 3d heat transfer in complex parallel heat exchangers using generalized graetz modes, J. Comput. Phys. 268 (2014) 84–105.

[18] J. Dichamp, F. de Gournay, F. Plouraboué, Theoretical and numerical analysis of counter-flow parallel convective exchangers considering axial diffusion, Int. J. Heat Mass Tran. 107 (2017) 154–167.

[19] P. Garibaldi, M. Misale, Experiments in Single-Phase Natural Circulation Miniloops With Different Working Fluids and Geometries, J Heat Transfer 130 (10) (08 2008).

[20] M. Misale, M. Frogheri, Stabilization of a single-phase natural circulation loop by pressure drops, Exp. Therm. Fluid Sci. 25 (5) (2001) 277–282.

[21] B. Swapnalee, P. Vijayan, A generalized flow equation for single phase natural circulation loops obeying multiple friction laws, Int. J. Heat Mass Tran. 54 (11) (2011) 2618–2629.

[22] Y. Jiang, M. Shoji, Flow stability in a natural circulation loop: influences of wall thermal conductivity, Nucl. Eng. Des. 222 (1) (2003) 16–28.

[23] P. Vijayan, M. Bade, D. Saha, R. Sinha, V. Venkat Raj, A generalised correlation for the steady state flow in single-phase natural circulation loops, Tech. rep., Bhabha atomic research center (2000).